



Deposited via The University of Sheffield.

White Rose Research Online URL for this paper:

<https://eprints.whiterose.ac.uk/id/eprint/182034/>

Version: Accepted Version

---

**Article:**

Monoranu, M., Mitchell, R.L., Kerrigan, K. et al. (2022) The effect of particle reinforcements on chip formation and machining induced damage of modified epoxy carbon fibre reinforced polymers (CFRPs). *Composites Part A: Applied Science and Manufacturing*, 154. 106793. ISSN: 1359-835X

<https://doi.org/10.1016/j.compositesa.2021.106793>

---

© 2021 Elsevier Ltd. This is an author produced version of a paper subsequently published in *Composites Part A: Applied Science and Manufacturing*. Uploaded in accordance with the publisher's self-archiving policy. Article available under the terms of the CC-BY-NC-ND licence (<https://creativecommons.org/licenses/by-nc-nd/4.0/>).

**Reuse**

This article is distributed under the terms of the Creative Commons Attribution-NonCommercial-NoDerivs (CC BY-NC-ND) licence. This licence only allows you to download this work and share it with others as long as you credit the authors, but you can't change the article in any way or use it commercially. More information and the full terms of the licence here: <https://creativecommons.org/licenses/>

**Takedown**

If you consider content in White Rose Research Online to be in breach of UK law, please notify us by emailing [eprints@whiterose.ac.uk](mailto:eprints@whiterose.ac.uk) including the URL of the record and the reason for the withdrawal request.

# *The effect of particle reinforcements on chip formation and machining induced damage of modified epoxy carbon fibre reinforced polymers (CFRPs)*

Marius Monoranu<sup>a,b,\*</sup>, Ria L. Mitchell<sup>c</sup>, Kevin Kerrigan<sup>d</sup>, J. Patrick A. Fairclough<sup>b</sup> and Hassan Ghadbeigi<sup>b</sup>

<sup>a</sup>Industrial Doctoral Centre in Machining Science, Advanced Manufacturing Research Centre, University of Sheffield, Rotherham, S60 5TZ, UK

<sup>b</sup>Department of Mechanical Engineering, The University of Sheffield, Sheffield, S1 3JD, UK

<sup>c</sup>Sheffield Tomography Centre (STC), The University of Sheffield, S3 7HQ, UK

<sup>d</sup>Advanced Manufacturing Research Centre, The University of Sheffield, Rotherham S60 5TZ, UK

\*Corresponding author. Tel.: +44-745-501-4034; E-mail address: m.monoranu@sheffield.ac.uk

---

## **Highlights:**

- Rubber and silica toughening mechanisms govern the chip formation process
- Cutting force evolution is different depending on the particle type and concentration
- Strain map contours indicated an extended deformation zone for silica modified samples
- Rubber modified samples experienced the lowest level of machining induced damage

## **Abstract**

The epoxy matrix of a carbon fibre reinforced polymer (CFRP) was modified by addition of silica nanoparticles, rubber microparticles and a combination of both to determine the effect of particle reinforcements on chip formation and machining induced damage. The effect of epoxy particle reinforcement on the machinability of CFRPs was studied experimentally under orthogonal cutting conditions. The results show that the chip formation process is affected by the presence of particulate fillers regardless of individual ply fibre orientation. Subsequently, the measured cutting forces showed a representative behaviour for each particle type and concentration. Rubber modified samples showed the lowest subsurface damage and measured surface metrics, followed by silica and unmodified epoxy samples. This behaviour was linked with the toughening mechanism of rubber and silica particles, which was found to take place during the material removal process.

**Keywords:** Nanocomposites; Particle-reinforcement; Damage mechanics; Machining

---

## **1. Introduction**

Multifunctional and multiphase materials, such as traditional carbon fibre reinforced composites, are designed to achieve greater functionality compared to their individual constituent materials. Coupling

individual material phases creates new hybrid materials with improved performance by reducing dimensions, weight, expense and energy consumption, while enhancing safety, design, and manufacturing versatility. A range of multifunctional and multiphase materials have been created by adding fillers into polymer composites [1]–[3]. The unique characteristics of micro and nano-fillers such as size, shape, mechanical properties and low concentrations necessary to create a beneficial change to the polymer matrix, together with the advancement in polymer characterisation and simulation techniques, have generated a great deal of interest in the field of modified polymer composites [4]. Nowadays, particle-modified composites are used in a wide range of industries including, but not limited to, aerospace [5], automotive [6], medicine [7], microelectronics [8], [9] and wind power [10]. Similar to conventional composite materials, particle-modified composites require features, such as holes and edges, to be generated via material removal processes after cure to achieve tight geometric tolerances and ensure edge-of-part mechanical performance. However, little information is available on their behaviour under such finishing operations. The complex nature of the interaction between cutting tool and fibre/matrix during machining of CFRPs and the difference in mechanical properties of fibre and epoxy-based polymer matrix can result in severe machining induced damage, including poor surface finish, matrix burn, pitting and delamination [11]–[13]. The ultimate effect of such defects is a potential reduction in the mechanical performance leading to catastrophic failure events [14].

Koplev et al. [15] studied the chip formation process in orthogonal cutting tests of unidirectional (UD) Carbon Fibre Reinforced Polymer (CFRP) laminates where the cutting process was considered to be a two-dimensional problem involving a tool edge perpendicular to the direction of the cut. It was concluded that the tool does not actually cut into the specimen, but the pressure that is applied into the fibres results in fibre breakage and matrix cracking leading to the chip formation, which is heavily dependent on the fibre orientation. Wang et al. [16] reported that chip formation varies with fibre orientation and to some extent with tool parameters. The same authors [17] concluded that an increase in the rake angle of the cutting tool results in smaller discontinuous chips resulting in improved surface quality. The general conclusion was

that the influence of cutting characteristics on the chip formation during an orthogonal cutting process is governed by the following, in descending order: fibre orientation, tool geometry and cutting parameters, such as cutting feed and speed [17].

Various fracture modes for different cutting tool configurations were identified by Arola and Ramulu [18] which concluded that rake angle and fibre orientation are key players in the chip formation process. It was also found that the defects and surfaces generated in multi-directional laminates had the same characteristics per ply as UD samples, indicating that the surrounding ply orientations had minimal effect on any individual ply. The “machinability” of UD CFRP laminates was further analysed in orthogonal cutting tests [19]. It was found that the subsurface damage is related to the depth of cut, fibre orientation and rake angle. An et al. [20] studied the cutting mechanics using the orthogonal cutting method. As the cutting speed increased, the main cutting force and thrust force decreased. The overall conclusion was that a suitable high cutting speed with appropriate cutting depth is helpful for stable machining of CFRP. Another study [21] investigated the effect of cutting speed on cutting mechanism of CFRPs. Results showed that with increasing cutting speed, fibre deformation and the affected area before fibre fracture decreased. Although the chip formation process in CFRPs and its mechanism have been well studied and reported in the literature, discussion of the effect of matrix properties and/ or particle-modified polymer matrix composites is limited.

Thakur and Singh [22] published a review on the influence of filler on polymeric composites during conventional machining, including drilling, milling and turning of composites with modified epoxy matrix using various fillers such as graphene, nanoclay, multi-walled carbon nanotubes (MWCNT), carbon nanotubes (CNT) and nano Silicon Carbide (SiC) particles. They reported that these fillers can be used to optimise machinability in terms of cutting forces, surface roughness and delamination depending on filler type, mechanical properties and physical characteristics. On the other hand, the reviewed papers lead to the conclusion that due to the complications in material removal process occurring during milling and turning,

the detailed explanation of chip formation with the application of fillers on polymer composite materials, needs to be investigated at a micro-scale.

The literature contains several studies which investigate the toughening mechanism and mechanical properties of a wide range of industrially available nanoparticles and microparticles, in particular silica and rubber, mixed in different epoxy blends and their composites [23]–[30]. However, from the machining point of view the available knowledge is generally limited to unmodified epoxy CFRPs.

The present work investigates the cutting behaviour of silica nanoparticles and carboxyl-terminated butadiene-acrylonitrile (CTBN) rubber microparticles modified epoxy CFRPs. The effect of fillers, at different concentrations blended into an epoxy matrix was assessed in relation to cutting force, chip formation, surface metrics and subsurface damage. This study provides fundamental work in the incorporation of micro and nano fillers in the epoxy matrix of a CFRP material, with an insight to the optimum cutting parameters needed to ensure low damage machining processes. Gaining understanding of chip formation process of modified polymer composites will enable designers and engineers a greater ability to introduce polymer-fillers during Design for Manufacture (DFM) stages of product design leading towards damage-free machining of high-value parts.

## 2. Experimental method

### 2.1 Resin and fillers

A low viscosity Diglycidyl ether of bis-phenol A (DGEBA) with an epoxide equivalent weight (EEW) of 167 g/eq (LY1564, Huntsman, UK) was used as the base epoxy resin together with a cycloaliphatic polyamine (Aradur 2954, Huntsman, UK) as the curing agent. Nano scale silica ( $\text{SiO}_2$ ) were supplied at a concentration of 40 wt. % in a DGEBA epoxy resin (EEW of 295 g/eq, Nanopox F400, Evonik, Germany). The reactive liquid carboxyl-terminated butadiene-acrylonitrile (CTBN) rubber was obtained as a CTBN-epoxy adduct with a rubber concentration of 40 wt. % in a DGEBA epoxy resin (EEW of 330 g/eq, Albipox 1000, Evonik, Germany). The DGEBA epoxy resin was mixed with the epoxy containing silica and/or

rubber particles to give the required concentration of nanoparticles. These blends were thoroughly mixed for 1 h at 400 RPM using a resin mechanical mixer and degassed in a vacuum oven at 60 °C. Six epoxy formulations were used as shown in Table 1.

**Table 1 - Epoxy formulations**

<b>Nanoparticles by weight (%)</b>	<b>Name</b>
Control	D (DGEBA)
10 % silica, 0 % rubber	Si10
20 % silica, 0 % rubber	Si20
10 % rubber, 0 % silica	R10
20 % rubber, 0 % silica	R20
10 % silica, 10 % rubber	Si10R10

## 2.2 CFRP panel manufacture and characterisation

CFRP panels were manufactured using a Hypaject Mk I RTM system. 14 plies of T300, 2x2 twill, 200 gsm, TC3091000 fibres (Sigmatech, UK) were stacked symmetrically about the mid-plane in a balanced manner to give  $[[((0,90)/(+45,-45))_3/(0,90)]_s$ , resulting in a panel of 300 x 300 x 3mm ± 0.05 mm . This lay-up was chosen to provide quasi-isotropic strength properties. The EEW of the epoxy blends were calculated and stoichiometric amounts of curing agent was added, mixed and degassed at 60 °C. The RTM mould was coated with 227CE release agent (Marbocoat, UK) before mixed resin was drawn into the RTM chamber and injected at 3 bars for 10 min, 4 bar for 10 min, 5 bar for 20 min and 6 bar for 20 min. Afterwards, the CFRP panels were cured for 1 h in the mould at 80 °C, removed from the mould and then post cured for 2h at 160 °C. Heating was at a rate of 2 °C/min.

In order to ensure the consistency of panels during manufacture, the glass transition temperature ( $T_g$ ) and fibre, resin and void content were all measured. A Perkin Elmer Pyris Diamond thermomechanical analyser (TMA) was used to measure  $T_g$  of the epoxy blends using rectangular block samples with dimensions of 12.5 x 3.5 x 3 ± 0.1 mm from cured epoxy sheets. The temperature was equilibrated at 25 °C at the start of the measurements and specimens were heated to 200 °C at 10 °C/min, while a constant force of 200 mN

was applied. The data was then analysed based on the method outlined in ISO 11359-3: 2019 [31] and the  $T_g$  was found as midpoint of the transition range using the first derivative of the dimension change versus measured temperature. A Perkin Elmer Diamond differential scanning calorimetry (DSC) was used to calculate the residual enthalpy change values,  $\Delta h$  of each manufactured panel to define degree of cure for the resin system. This ensures that the same degree of resin/ hardener cross-linking has occurred between each panel regardless of the concentration and reinforcement particle used.

Two sections from each panel were cut to determine the fibre-volume fraction prior to machining to ensure a similar content across all panels was achieved. The samples were prepared according to Ashworth et al. [32] and the ratio of matrix, void and fibres was calculated through analysis of five different pictures using ImageJ software (LOCI, University of Wisconsin, USA). The measured values were averaged and reported for further investigations.

### 2.3 Orthogonal cutting tests

The chip formation process was investigated in orthogonal cutting conditions using a specially designed rig attached to a Tinius Olsen 25ST benchtop tester. Further details about the cutting rig working principles and dimensions are available in the literature [33]. The enclosed setup of rig allows the observation of the cutting process under 2D plane strain conditions. The cutting process was recorded using a High Speed 2D Digital Image Correlation (DIC) system (LaVision, GmbH) paired with a Navitar 12x Zoom Lens system with the parameters as shown in Table 2. The cutting forces were measured using a Kistler 9257B dynamometer at an acquisition rate identical to the imaging frequency of 10 kHz. The force and imaging frequency were synced to correlate the observed phenomena during the cutting process.

A Protomax (Omax, USA) Abrasive water jet (AWJ) machine was used to cut the samples to the required size of 25 x 25 mm. CFRP panels were submerged 1mm under water during cutting. The water pressure and feed rate of the nozzle was determined by type and thickness of the material and a level of desired surface quality. The same water jet and cutting parameters were used in a previous study by Monoranu et

al. [14] where similar material was cut and machining induced damage due to AWJ process was identified. The machined side of the samples were further polished using P400 grit paper to remove any machining induced damage.

DIC speckle patterns were applied using a fine coat of white paint and speckle pattern was created by spraying copier toner powder using a dust atomizer (Goodson, USA). The cutting tests were repeated 8 times for each sample to ensure on the consistency of the results. A cutting speed of 1000 mm/min was used, which is the maximum speed that the tensile machine can achieve. The depth of cut was set to 200  $\mu\text{m}$  to be able to clearly capture the strain developing during the chip formation process. The depth of cut was measured using a digital micrometer, with a resolution of 1  $\mu\text{m}$ , attached at the side of the rig and further checked via the calibrated imaging system. High-speed steel cutting inserts with a rake angle  $\alpha=10^\circ$ , clearance angle  $\gamma=10^\circ$  and edge radius  $r=10 \mu\text{m}$  were used. The cutting tools were replaced regularly to ensure the cutting performance was not affected by the tool wear. The cutting tools were manufactured using precision grindings and geometrical features of all the tools were measured using an optical focus variation system, Alicona Infinite Focus SL and 2.7% variation in the cutting edge radius was recorded.

**Table 2 – High Speed 2D DIC parameters**

Parameter	Value
Technique	2D High Speed DIC
Software	Davis 10.1
Subset size	29 x 29 pixels
Step size	9 pixels
Camera	Phantom V410L
Lens	Navitar 12x Zoom Lens system
Image resolution	796 x 1277 pixels
Field of view	1.025 x 1.644 mm
Frame rate	10 kHz
Spatial resolution	0.11 mm

#### 2.4 Post machining assessment of surface integrity

Areal surface scanning was conducted using an Alicona Infinite Focus SL optical focus variation system at 20x magnification. Exposure was set to 7.25 ms, contrast set to 0.7 with vertical resolution, and lateral

resolution set to 400nm and 1 $\mu$ m. An area with a length of 6 mm on the machined side of the samples was scanned covering 6 x 3 mm<sup>2</sup> with 3 mm being the thickness of the sample. A cut off length  $\lambda_c$  of 0.8 mm was applied to the image before spatial and autocorrelation textural parameters were collected from Alicona IFMeasurement Suite as per ISO 25178 [34]. Profile data was collected and measured according to ISO 4288 [35] and ISO 3274 [36] specifications. For profile measurements, five measurements were taken in the transverse cutting direction across the full thickness of 5 samples and the average value was used for analysis purposes.

A FEI Inspect F SEM (Hillsboro, Oregon, USA) was used to assess the machined surface morphology at high magnifications. Samples were gold sputter-coated prior to the SEM microscopy. SEM micrographs were taken at 5kV accelerator voltage and a level 2 spot size to obtain the required resolution for the imaging features of interest on the surface of the machined samples.

The machining induced subsurface damage was characterised in 3D using a Zeiss Xradia Versa 620 X-ray Microscope (Pleasanton, Ca, USA) housed within the Sheffield Tomography Centre (STC) at the University of Sheffield, UK. This method was utilised specifically for non-destructive 3D imaging. The sample was glued to a cocktail stick and screwed onto one of the Versa sample mounts to ensure it did not move during the scan. X-rays were generated from a tungsten transmission target and collected on a CCD (charge coupled device) 16bit 2000 x 2000 pixel detector camera. Five samples were scanned under varying conditions; X-ray tube voltages ranged between 50 and 60 kV, tube currents between 90 and 108  $\mu$ A, source power between 4.5 and 6.5 W, and exposure times between 2 and 3 seconds per projection. 1601 projections were collected for each scan over a scan time of 2 hours. On the whole, inserting a filter to filter out low energy X-rays was not necessary; however, a filter (LE2) was inserted for some scans. Variable scan conditions were needed because of variations in sample thickness, meaning X-ray penetration was more difficult for the thicker samples and required a higher power. For all scans an objective lens was used giving an optical magnification of 4x, while binning was set to 2 producing an isotropic voxel (3D pixel) size of 2.5  $\mu$ m at a field of view of 2.5 x 2.5 mm for each scan. A filtered back projection method was used

to reconstruct the data, and the reconstructed images were converted to 8bit greyscale 2D .tiff stacks using Zeiss Scout and Scan Reconstructor software. The Scout and Zoom methodology was used to create targeted high-resolution regions of interest (ROIs) from lower resolution scans (at  $\sim 10 \mu\text{m}$  voxel size), which were also collected. 3D volume information was segmented and visualized in Dragonfly, a specialised tomographic software (Object Research Systems, Montreal, Canada).

### 3. Results and discussion

#### 3.1 CFRP material characterisation

Table 3 shows the measured fibre, resin and void content by % of volume along with glass transition temperature and degree of cure. The void content for all panels is low (average of 1.51 %) which is typical for the RTM process.  $T_g$  of the panels is  $151^\circ\text{C}$  with a panel-to-panel variation of  $\pm 2.3^\circ\text{C}$  ( $\sim 1.5\%$ ). The degree of cure results, which varied by only 0.3% across all specimens, indicate that all CFRP panels were fully cured regardless of the particle concentration used. Overall, characterisation results show that the epoxy blends used in the manufacturing process provided panel consistency. This ultimately demonstrates that experimental variation due to the condition of material have been largely mitigated. It is therefore unlikely that any results obtained relating to chip formation or surface quality are due, in any significant part, to such material variations.

**Table 3 – Material characterisation results for modified and unmodified epoxy CFRP specimens**

Sample name	Fibre content (%)	Matrix content (%)	Void content (%)	( $T_g$ ) TMA $^\circ\text{C}$	Degree of cure (%)
DGEBA	$64.88 \pm 0.79$	$33.99 \pm 0.56$	$1.12 \pm 0.24$	152.6	99.3
R10	$64.36 \pm 1.20$	$34.09 \pm 1.23$	$1.56 \pm 0.16$	152.1	99.1
R20	$63.77 \pm 0.84$	$33.99 \pm 0.59$	$2.24 \pm 0.24$	151.1	99.2
Si10	$65.86 \pm 0.82$	$33.15 \pm 0.63$	$0.99 \pm 0.21$	150.2	99.4
Si20	$65.42 \pm 0.92$	$32.51 \pm 0.67$	$2.07 \pm 0.26$	151.3	99.2
Si10R10	$66.04 \pm 0.22$	$32.84 \pm 0.18$	$1.13 \pm 0.14$	150.7	99.3

### 3.2 Effect of matrix type on cutting force evolution

Figure 1 – a) shows the average values of measured cutting forces for each material together with standard deviation error bars. Unpaired T-statistical tests were run to compare the difference between the cutting force magnitudes, and it was found that adding the particulate fillers will result in statistically significant differences in cutting forces between unmodified (DGEBA) and modified samples. A 20.2% decrease was found for R10, followed by a further 42.4% for R20 samples compared to DGEBA. The Si20 samples showed a decrease of 14.2% in cutting force magnitude, while ‘hybrid’ sample (Si10R10) showed a decrease of 24.1%. It is noticed that Si10R10 had similar cutting force magnitude to R10 specimens, which suggests that in a ‘hybrid’ composite the rubber microparticles are governing the material removal process.

The amount of spring back was measured after each cut using a digital micrometre (resolution  $< 1 \mu\text{m}$ ) and further checked using the recorded cutting images as shown in Figure 1- b). The brittle-matrix epoxy represented by unmodified (DGEBA) and silica epoxy (Si10, Si20) experienced the lowest elastic recovery and highest cutting force. On the other hand, the presence of rubber microparticles (R20) increased the elastic recovery and the lowest cutting forces were recorded. The increased elastic recovery due to rubber particles is related to toughening mechanism and large strain to failure of rubber modified composites [28], [37], [38]. Additionally, the decrease in the cutting forces is correlated with a smaller volume of material removed, despite the large elastic deflection. Wang and Zhang [19] reported that in orthogonal cutting of UD-CFRPs the magnitude of spring back is related to the cutting edge radius of the tool, when all the other conditions are the same. Considering that all the cutting parameters in this study, including the tool geometry and cutting conditions are identical between the investigated samples, the observed trend in the measured spring back could only be due to the local mechanical properties of the modified epoxy matrix indicating that the presence of fillers has a significant effect on spring back. A difference of  $16 \mu\text{m}$  was found between the largest springback distance (R20 sample) and lowest value (Si20 sample) as shown in Figure 1 – b).

The evolution of cutting forces as the cut progresses (Figure 2) indicates that there is less variation in the cutting force when cutting rubber modified samples, while a large oscillation was observed in the graphs related to the reference material (DGEBA) and the silica-modified samples (Figure 2 – a)). The cutting force signal for R10 and Si10R10 samples (Figure 2 – b)) showed a similar pattern. This was previously observed in orthogonal cutting of rubber and silica modified epoxy polymers [39], where the chip formation process was mainly influenced by the presence of rubber microparticles, rather than silica nanoparticles in the ‘hybrid’ sample. It has been previously reported [28] that in a ‘hybrid’ modified CFRP, the rubber toughening mechanism is the dominant failure mechanism. This aspect and the effect of chip formation process in relation to particulate fillers and cutting force behaviour is further discussed in Section 3.3.

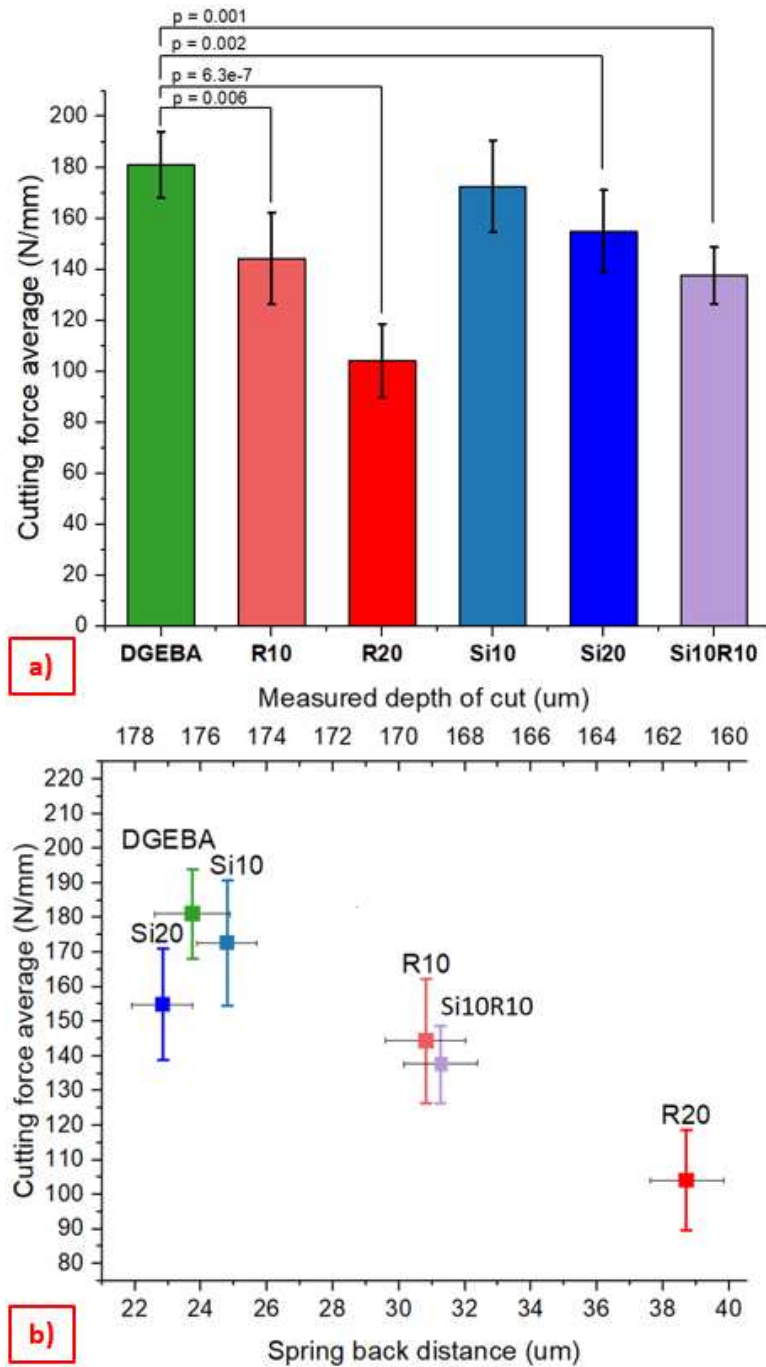


Figure 1 - Cutting force analysis graphs with error bars representing standard deviation of the test samples a) Cutting force average (only p-values which are statistically significant values are shown) b) Cutting force average vs spring back distance & actual depth of cut

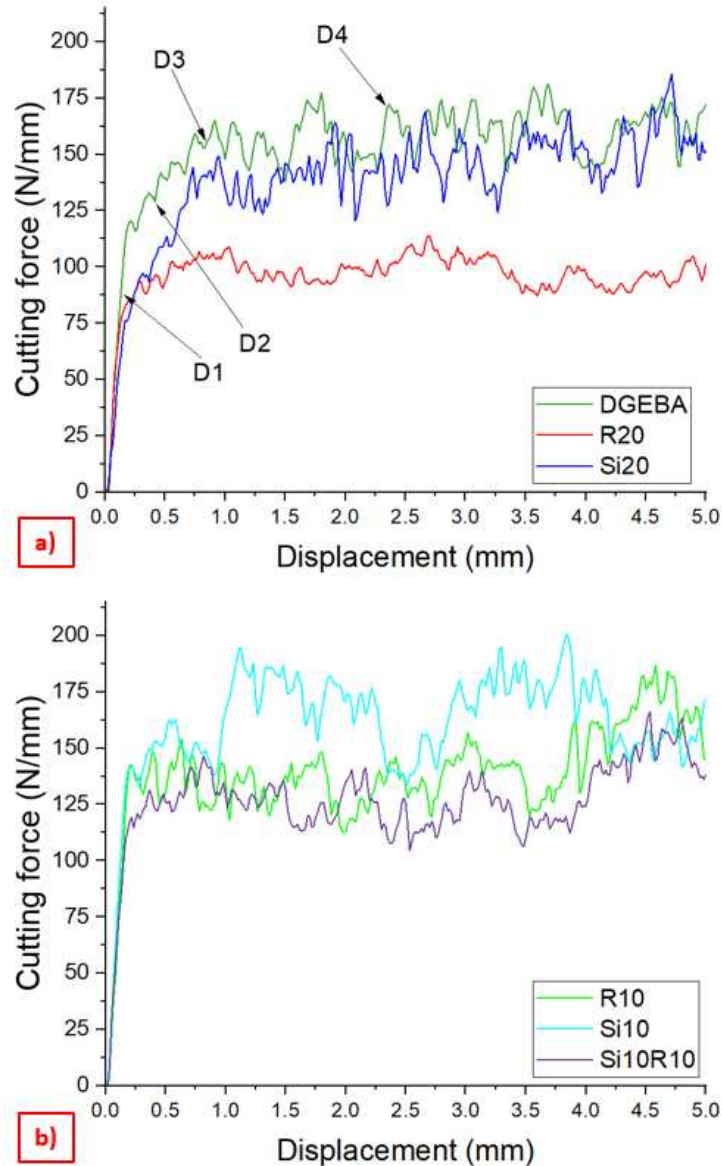


Figure 2 - Cutting force vs displacement for a) DGEBA, R20 and Si20 where D1, D2, D3, D4 indicate the time steps corresponding the cutting images in Figure 3, and b) Cutting force vs displacement for R10, Si10 and Si10R10

### 3.3. Analysis of chip formation in relation to cutting forces and strain evolution

Figure 3 shows the evolution of chip formation from the side view of the samples during cutting as observed by the High Speed DIC system where the individual frames are correlated to the time steps shown in the force-displacement diagram of Figure 2 – a). As the tool advances into the work piece, the fibres at  $0^\circ$  are compressed (shown by curved dash line of Figure 3– b)) and by further displacement of the cutting edge a chip forms on the rake face of the cutting tool (Figure 3 – b)). Relaxation and material recovery occurs at

the flank side of the tool (shown by straight dash-dot line in Figure 3 – b)). The material pile on the rake face of the tool and a continuous chip is formed, while  $0^\circ$  fibres are bending and fracture in front of the cutting tool (Figure 3 – c)). This is primarily due to the low cutting speed and high bending limit of the  $0^\circ$  fibres used for this experiment. Considering the 2x2 twill woven fibre architecture of the samples (carbon fibre placed in a  $0/90^\circ - 45/135^\circ$  configuration with  $0/90^\circ$  on the top/ bottom plies), the tool will encounter  $0^\circ$  and  $90^\circ$  fibres on the top plane as the sample is cut. As the tool enters a region with  $90^\circ$  fibre orientation, large cracks ( $>500 \mu\text{m}$ ) are generated in the matrix between fibres on the top ply (Figure 3 – d)) due to excessive bending of fibres along their axis. These long cracks are only present on the top ply, as fibres can readily deform-out of plane and cracks are formed from a combination of bending and debonding from the matrix. CT-scan images did not show these features on the layers below the surface. This aspect is further discussed in Section 3.4. No noticeable difference was found between side view images of the particle-modified samples and DGEBA specimen, the chip formation process shows the same behaviour.

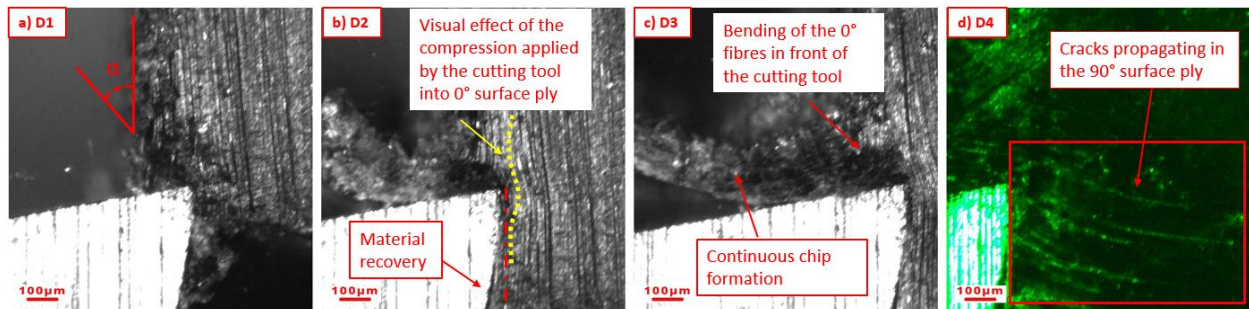


Figure 3 - Chip formation process images a-d) corresponding to the selected time steps of D1-D4 Figure 2 – a), d) D4 has a false colour black-green contrast to highlight the surface ply crack propagation for  $90^\circ$  fibre orientation

Strain maps shown in Figure 4 and 5 are linked to the cutting force signal of Figure 6. Maximum normal strain (MNS) and shear strain (SS) have been calculated for each test condition according to the parameters given in Table 2 and represent the onset of steady state cutting zone (Figure 4 and 5 – a), c), e)) and full engagement of the cutting tool with the material which starts to build up on the rake face of the cutting tool (Figure 4 and 5 – b), d), f)). MNS maps of DGEBA (Figure 4 – a)) showed a larger deformation zone compared to rubber modified samples (Figure 4 – c)) in which strain contours are situated close to the cutting tool. On the other hand, Si20 sample had the lowest MNS value of 0.11 [S], followed by R20 sample

with 0.27 [S] and DGEBA with 0.45 [S]. Si20 sample (Figure 4 – e)) showed a more localised strain map, which is linked to the stiffness of the silica nanoparticles. As the material is deformed due to further penetration of the cutting tool, the local strain values increase for all samples, while strain contours are still localised in front of the cutting tool for R20 and Si20 samples ((Figure 4 – d, f)). DGEBA sample (Figure 4 – b)) shows the highest MNS value of 1.1 [S], however the strain contours are dispersed around the cutting tool in two zones: (i) one that is extended ahead of the cutting tool (ii) one that penetrates approximately  $45^\circ$  into the subsurface. The high value of MNS of DGEBA sample and the strain contours dispersion is attributed to the deformation and fracture of the material. In the case of rubber modified sample, toughening mechanism took place [28], [37], which increased the plastic zone ahead of the cutting tool, hence limiting the fracture and deformation of material. SS maps (Figure 5) show a compression area (negative value of SS) formed across the relief face of the tool, while a tensile area (positive value of SS) is formed on the rake face. Similar to MNS contours, R20 sample (Figure 5 – c, d)) showed the SS contours distributed close to the cutting tool edge. On the other hand, silica sample (Figure 5 – e, f)) experienced the largest compression deformation zone. The increased stiffness of the silica particle should make a contribution to the load carrying capacity of the composite, however, the stress concentration effect due to presence of silica nanoparticles weakens the material [29]. The effect of particle toughening and failure mechanism which occurs during the material removal process is further discussed in Section 3.6.

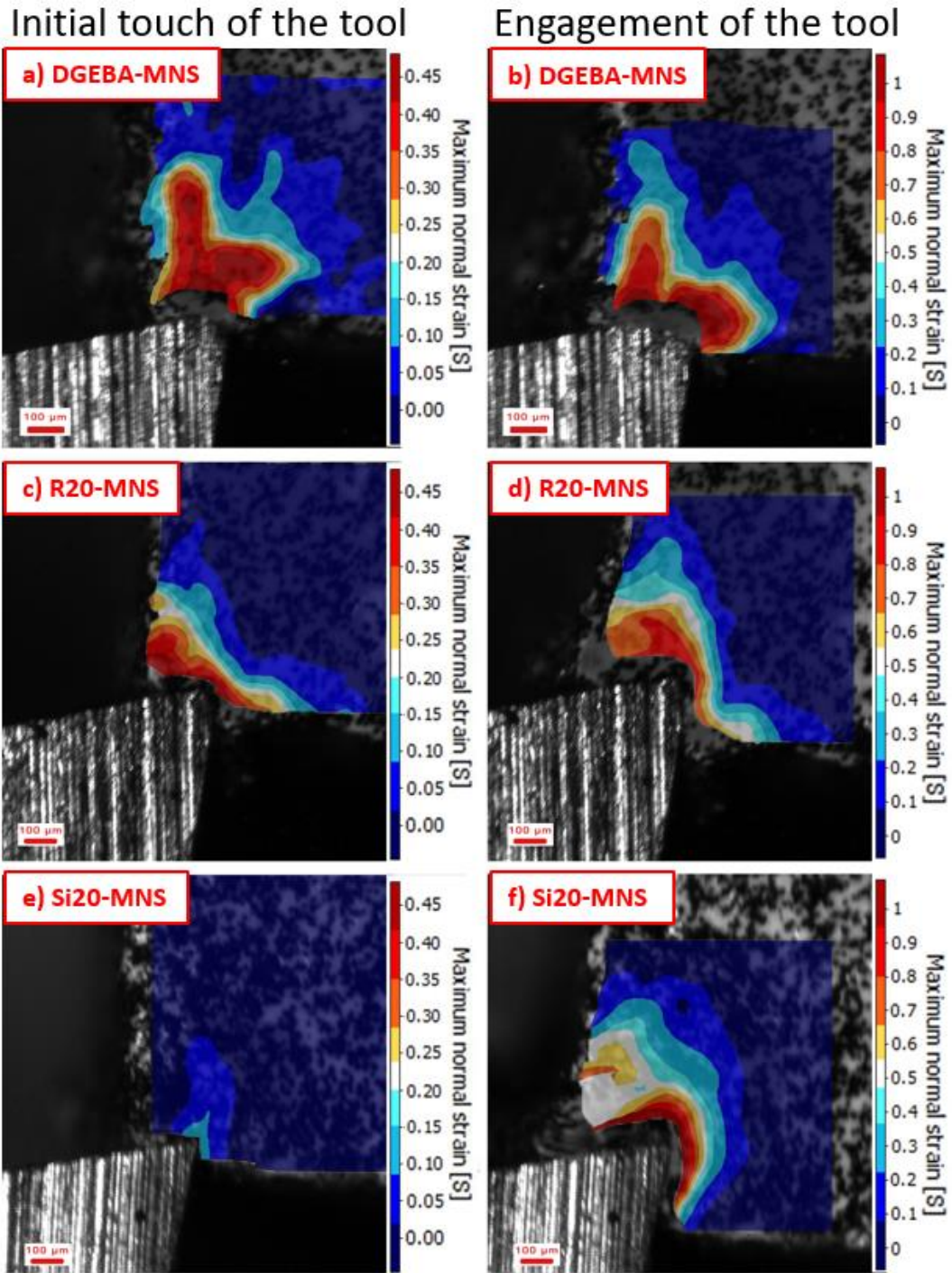


Figure 4 - Maximum normal strain [S] (MNS) maps for a - b) DGEBA c - d) R20 e - f) Si20 corresponding to the time force points marked a - f on Figure 6

Initial touch of the tool

Engagement of the tool

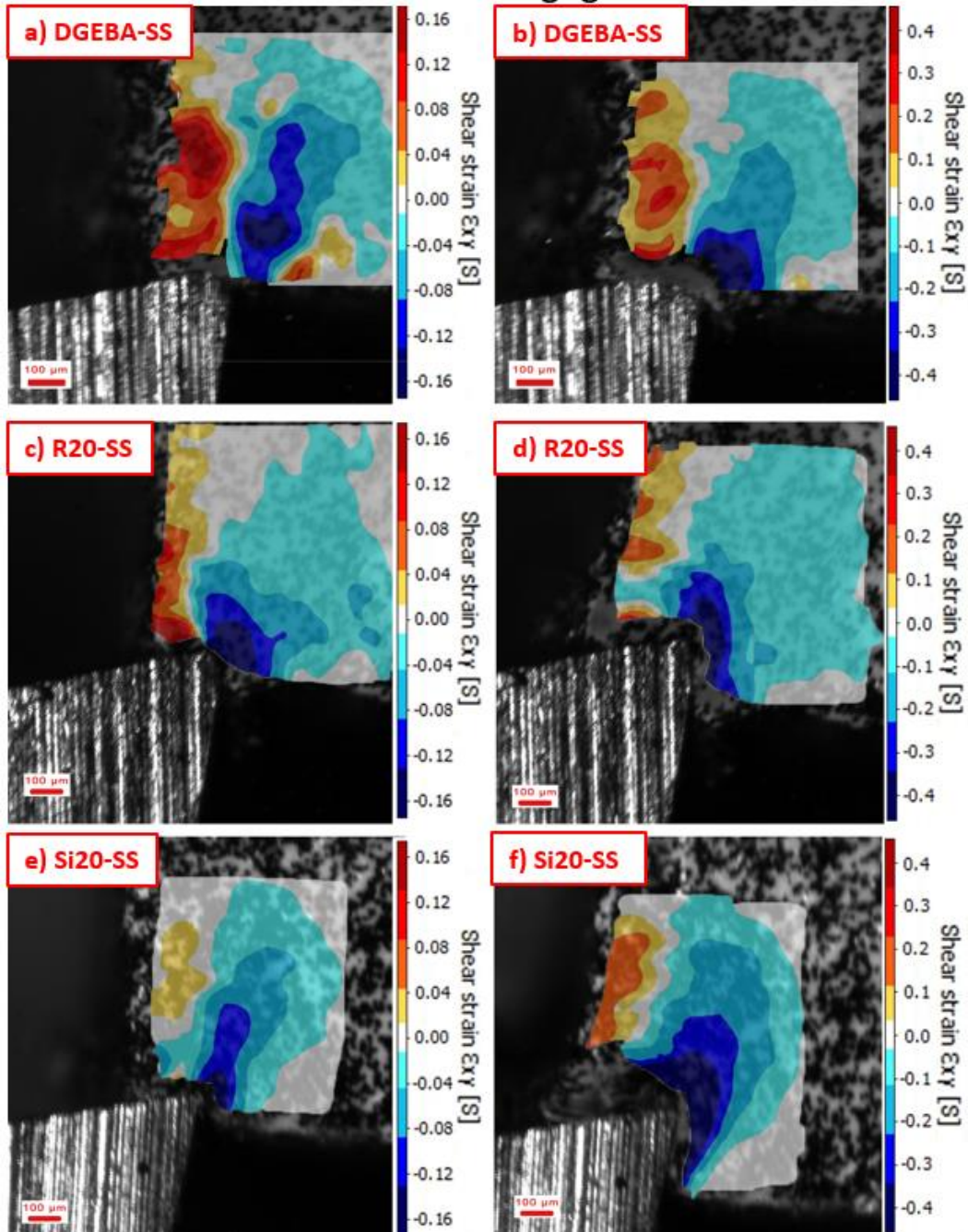


Figure 5 - Maximum shear strain [S] (SS) maps for a - b) DGEBA c - d) R20 e - f) Si20 corresponding to the time force points marked a - f on Figure 6, with negative values corresponding to compression force due to the flank face compression

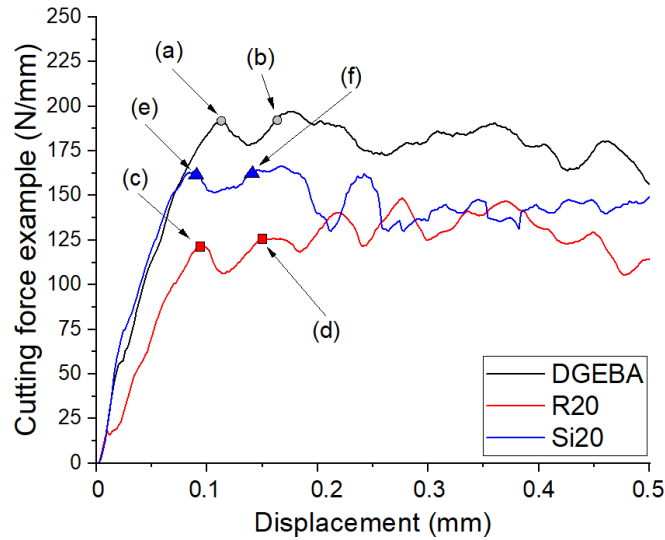


Figure 6 - Cutting force vs displacement for D, Si20 and R20 samples where (a) – (f) have corresponding time stamps to equivalent strain maps of Figure 4 and 5

### 3.4 Subsurface damage analysis in relation to chip formation mechanism for individual plies and fibre orientations

The cutting process was interrupted in the middle of the cut and the sample was analysed with 3D micro-CT to quantify the subsurface damage both under the machined surface and ahead of the cutting tool during the chip formation process as shown in Figure 7. 2D slices were extracted for processing from the middle of the specimen ensuring that the chosen part of material was cut in plane-strain conditions. The subsurface damage was quantified in terms of maximum damage depth and area of damage. As we cannot discriminate between damage induced by the cutting edge or damage from compression due to the flank face, then damage refers to any type of defect which is induced by the orthogonal machining process. Depending on the fibre orientation, this can include matrix cracks, fibre breakages, fibre bending, matrix/ fibre pull-outs and uncut fibres. A MATLAB® script [40] was used to calculate the damage area. The volume of indentations (craters) observed on the 135° plies was calculated using the Dragonfly CT segmentation software (Figure 7 – b)). These have previously reported during machining of CFRPs [12], [13] and it was found that they adversely affected the mechanical properties of the samples namely flexural and compressive strength [14], [41], [42].

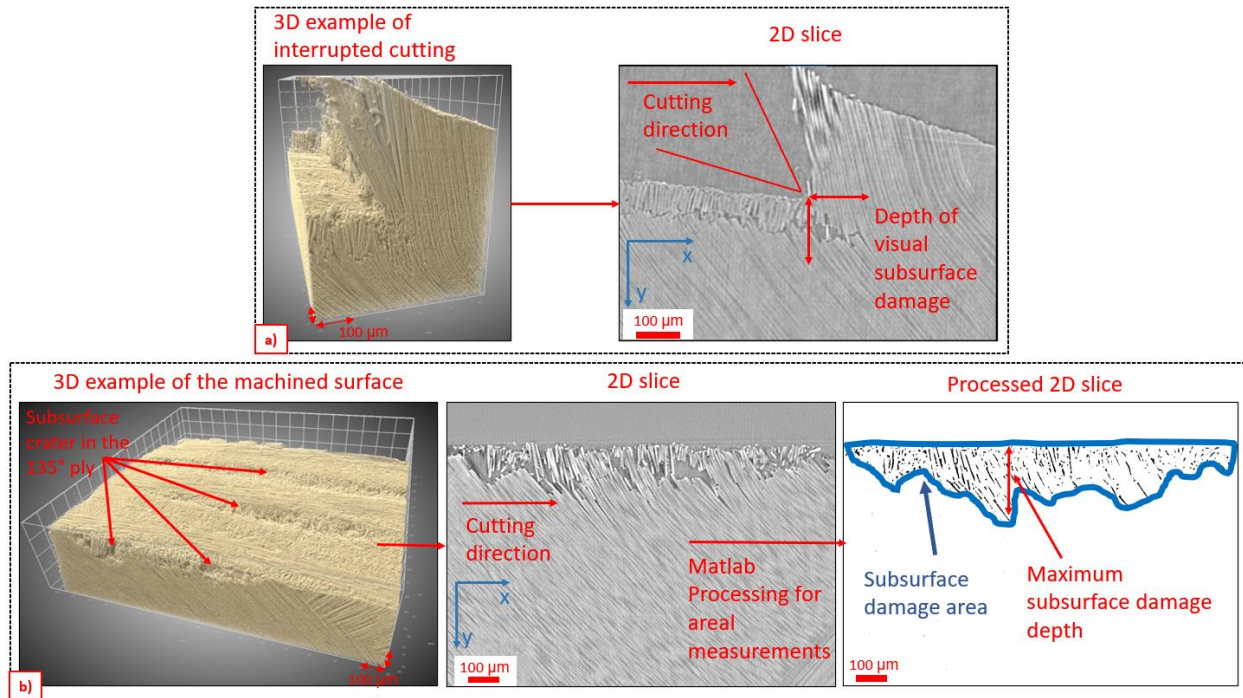


Figure 7 – a) Subsurface damage measurement example of DGEBA sample for chip formation process in an interrupted cutting  
 b) Subsurface damage assessment

All the machined surfaces showed significant matrix smearing across all fibre orientations. Figure 8 shows the calculated subsurface damage for the machined materials. For a single material, changing the fibre orientation from  $45^\circ$  to  $135^\circ$ , shows an increase in the damage area. However, within an individual fibre orientation, defined by a ply layer, the addition of rubber or silica fillers results in reduced subsurface damage. The calculated maximum subsurface damage depth (Figure 8 – a)) shows a decrease for all fibre orientations when silica or rubber was added to the epoxy matrix. Moreover, the R20 sample had the lowest level of damage, which can be attributed to rubber toughening mechanism which is active during material removal. Experimental evidence is discussed in Section 3.6. Moreover, damage in front of the cutting tool, areal damage and crater volume has the lowest values for the R20 samples. An increase in damage in front of the cutting tool was found for Si20 sample in the  $90^\circ$  fibre orientation, however the measured values are within the standard deviation of the control. No quantifiable surface intrusion or subsurface damage was identified for  $0^\circ$  fibres, therefore Figure 8 does not include  $0^\circ$  orientation in damage comparisons.

The measured subsurface damage is further explained when considering fibre orientation and the fracture mechanism, based on the 2D interrupted cutting images (Figure 9) and the representative subsurface damage examples (Figure 10). The cutting mechanism in the multidirectional ply laminate is similar to the UD laminate, with a slight difference in the  $90^\circ$  and  $135^\circ$  fibre orientation as the result of the influence from adjacent plies as previously discussed by Arola and Ramulu [16]. Excessive out-of-plane damage in multidirectional occurs at  $90^\circ$  or greater in UD laminates, while the damage in multidirectional laminates, at these angles, is limited due the support of adjacent plies. This facilitates the analysis of the material removal mechanism for each ply and fibre orientation based on analogous UD laminates.

According to [43] the cutting mechanism can be grouped as Type I, III, IV and V chip formation process depending on the fibre orientation. Type I chip formation describes  $0^\circ$  fibre cut via crack propagation ahead of the tool where the fibres are peeled from the surface then bend and fracture (Figure 9 – a), b), c)). Fibres on the machined surface fracture perpendicular to their long axis due to the compression from the cutting tool applied against the front surface. For  $0^\circ$  fibre orientation, the reinforcement particles did not show any noticeable effect on the chip formation process or subsurface damage.

Type III is typical for  $45^\circ$  fibre orientation where chip formation consists of fracture from compression-induced shear across the fibre axis followed by interlaminar shear fracture along the fibre-matrix interface as the tool advances into the material. The shearing mechanism at the fibre-matrix interface is clearly visible in Figure 9 – d), e), f). During the compression stage of the material removal mechanism, fibres are fractured, and cracks are generated below the cutting plane as shown in Figure 10 – d), e), f). The extent of damage is limited for the R20 sample compared to the other samples which is also shown quantitatively by graphs of Figure 8 – a), b), c). This is associated with the presence of rubber particles, which makes the fracture less brittle, therefore, less energy is dissipated in the fracture resulting in a limited damage. This is also observed in Figure 6, where i) the cutting force in rubber has the smallest value and ii) there are more constant chips formed (based on the wavelength shape and dips in the force curve).

As the fibre orientation increases to  $90^\circ$ , interlaminar shear increases, leading to the fracture of the fibre and fibre and the matrix. The compressive stress within the contact region between cutting tool and fibre will reach the failure value of fibres at a small deformation or movement of the fibre. This is typical for Type IV chip formation process. Fibres fracture at the tool tip position for R20 sample (Figure 9 – i)) or a crack is developed on the cutting plane in front of the cutting tool (Figure 9 – g), h)). The crack propagation in front of the cutting tool is facilitated by the brittle state and low fracture toughness of silica and unmodified epoxy compared to the rubber modified sample. Similar to  $45^\circ$  fibre orientation, the presence of rubber particles reduces the fibre crushing effect. Unmodified epoxy composite showed a continuous line of subsurface fracture fibres (Figure 10 – g)) which are suspected to fail due to excessive bending as the cutting tool advances into the material. Crushing-dominated fibre fracture is replaced by bending-dominated fibre fracture when a large cutting edge radius of the cutting tool is adopted [44]. However, in this study, the cutting tool edge radius is the same for all machined samples. Moreover, subsurface bending fracture in the  $90^\circ$  laminate plane is difficult to achieve due to the strong constraining effect of the neighbouring fibres [44]. Therefore, it is assumed that the matrix-fibre interface starts to debond as the surface contact pressure is building up with the motion of the tool, which will lead to bending and fracture of the fibres at subsurface level. The interface failure aspect is further discussed in Section 3.6 where high-magnification SEM micrographs are used as experimental evidence.

In Type V for  $135^\circ$  fibre orientation, bending is caused by flank face compression – as the tool advances of the cutting tool into the material. This causes the matrix to crack and fibres to fracture (Figure 9 and 10 – k), l), m)). This further results in material becoming detached and allowing material to pull-out, which leads to the formation of craters below the cut surface. The calculated crater volumes are shown in Figure 8 – d). A 50.8 % decrease is found between R20 and DGEBA samples, while the subsurface damage area and maximum damage depth for  $135^\circ$  plies decreased by 63 %, and 25 %, respectively. These results are linked with the high fracture toughness of the rubber modified epoxy, limiting the crack growth along the matrix in  $135^\circ$  fibre orientation, thus decreasing the amount of pull-out material and subsurface damage.

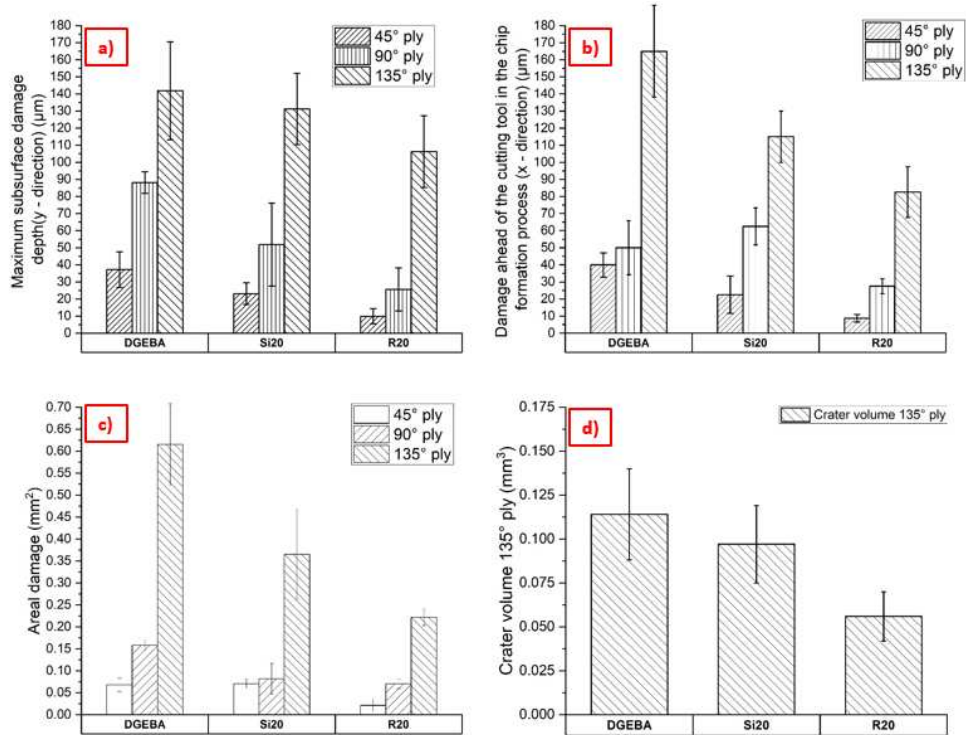


Figure 8 - Subsurface damage assessment with error bars showing the standard deviation of the assessed images a) Maximum subsurface damage b) Damage in front of the cutting tool c) Areal damage d) Crater volume (0° fibre orientation did not show damage by these measurements)

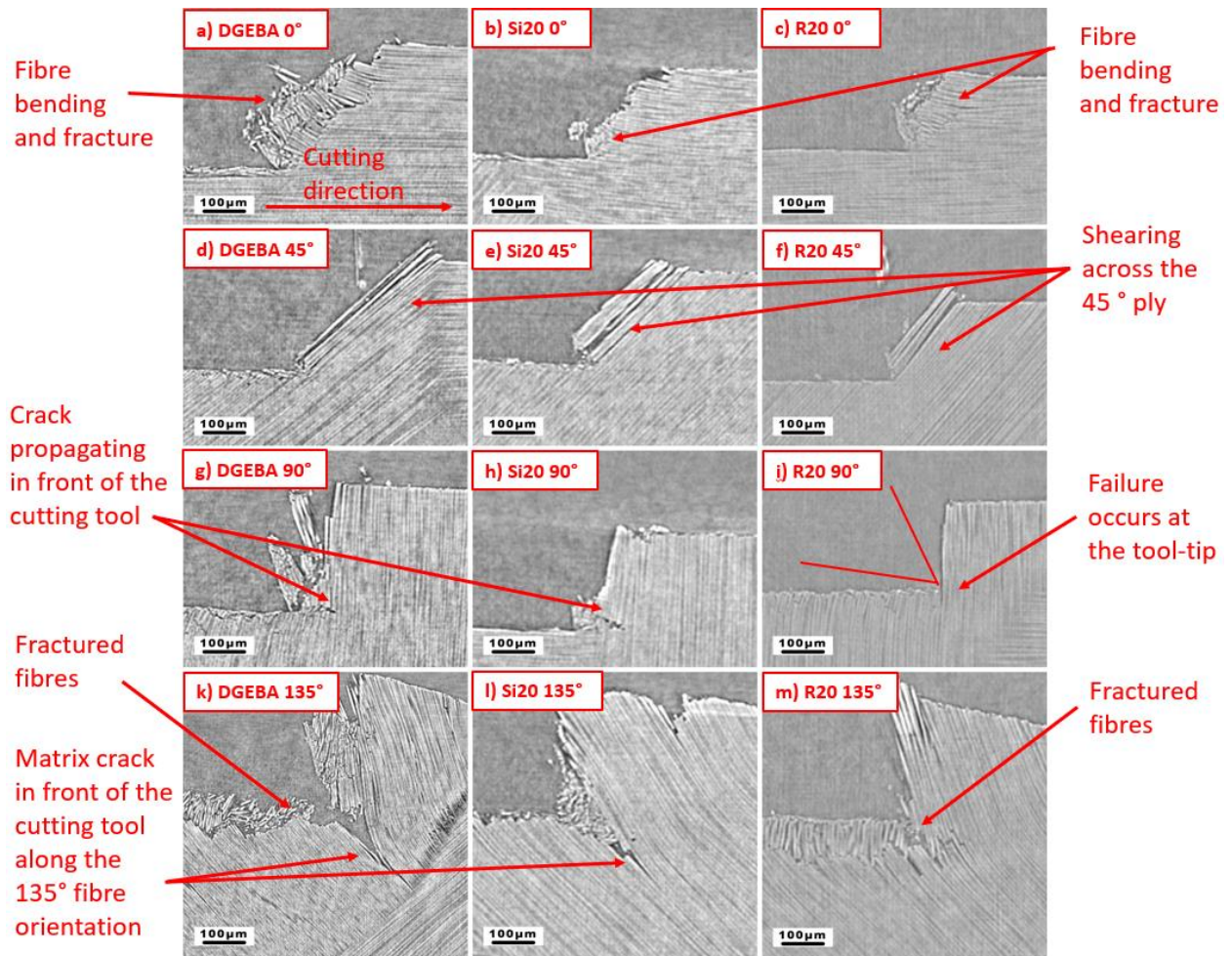


Figure 9 – 2D slice examples of interrupted cutting for DGEBA (a, d, g, k), Si20 (b, e, h, l) and R20 (c, f, i, m) samples showing machining induced damage

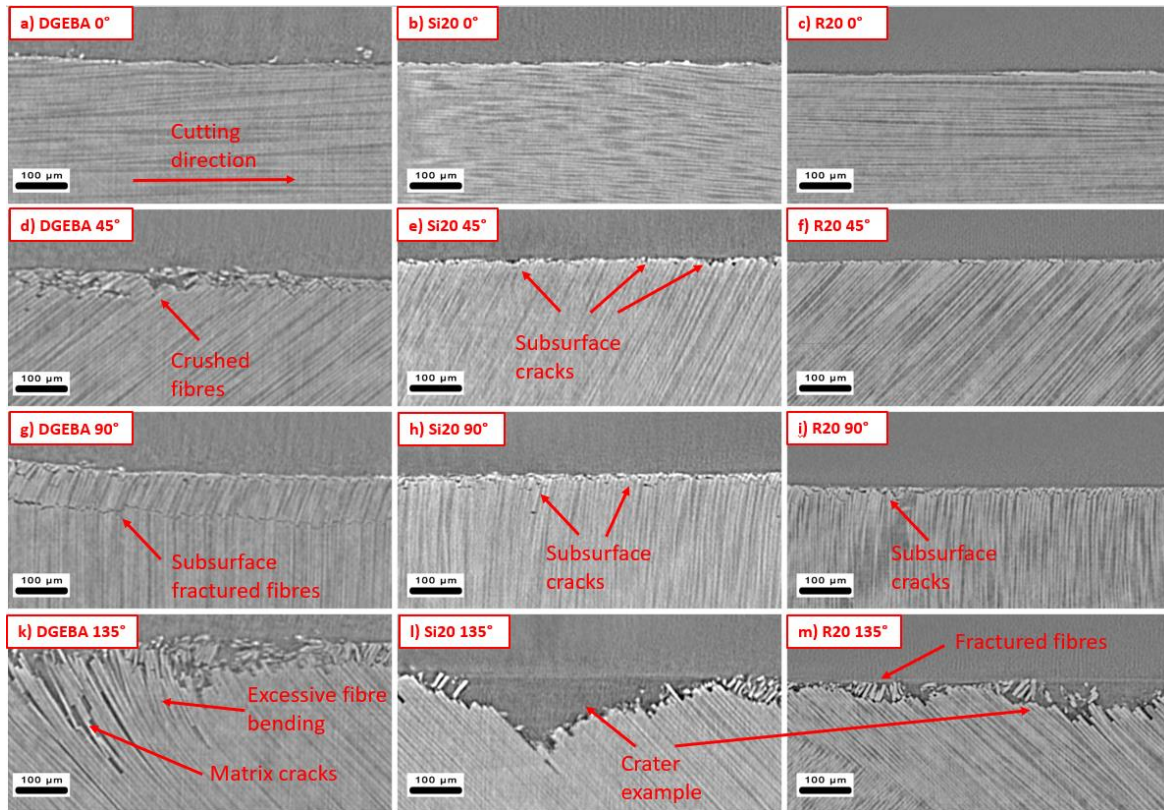


Figure 10 – 2D slice examples of subsurface damage for DGEBA (a, d, g, k), Si20 (b, e, h, l) and R20 (c, f, i, m) samples

### 3.5 Machined surface characterisation

Figure 11 shows the variation of selected metrics to investigate machined surfaces in the samples. Due to waviness and twill-weave architecture of the carbon fibre plies of the CFRP material, individual ply surface topography analysis was not possible; hence, measurements across the full-machined surface were used. As shown in Figure 10 and previously in the literature [12], [13], [40], fibre orientation has a strong influence on the generated surface topography after machining. DGEBA samples represent the reference material in Figure 11. As the rubber content increases (Figure 11 – a)), the  $S_a$  (average height of scanned area) parameter decreases.  $R_a$  parameter (average roughness of profile) shows a similar trend, however it is reported that  $S_a$  provides greater reliability of roughness measurement for multidirectional laminates [45]. Adding silica nanoparticles from 10% to 20% wt. causes  $S_a$  to increase. These have been balanced in the ‘hybrid’ Si10R10 sample which contains 10% silica and 10% rubber. A similar trend was found for the  $S_v$  (maximum valley depth of scanned area) measurements Figure 11 – b). Interestingly, Si10R10 sample

showed the lowest  $S_v$  value (Si10R10:  $S_v$  - 42), followed by rubber (R20:  $S_v$  - 61), silica (Si10:  $S_v$  - 63, Si20:  $S_v$  - 92) and DGEBA sample (DGEBA:  $S_v$  - 102). CT-scan images (Figure 10 – k, l, m)) showed that the maximum depth of damage occurs in the 135° fibre orientation plies and surface metrics are measured on the entire surface of the specimens, therefore the measured  $S_v$  values are attributed to the 135° plies. However, it is noted that maximum depth of subsurface damage (Figure 8 – a)) is 35 – 40 % higher than  $S_v$  measurements (Figure 11 – b)). This is accounted for by the fractured fibres and matrix which were not completely pulled out and remained on the bottom of subsequently generated craters, hence influencing the topography measurements (example in Figure 10 – k, m)). This highlights the fact that surface metrics assessment of the machined surfaces is insufficient to characterise machining induced damage.

The variation of surface Kurtosis ( $S_{ku}$ ) and surface Skewness ( $S_{sk}$ ) parameters (Figure 11 – c), d)) show that DGEBA and silica modified composites (Si20) had the highest value of Kurtosis indicating a surface with sharp peaks and valleys. A negative Skewness was found for all samples, which is a characteristic of a surface with deep cracks and voids. This type of features is typical for 135° plies, as CT results (Figure 10) showed no similar features for the other fibre orientations. Similar to subsurface damage results discussed in Section 3.4, R20 experienced the lowest  $S_{sk}$  value (Figure 11 – d)) which is correlated with limited material pull-out that is linked with the rubber toughening mechanism, followed by silica and unmodified epoxy composite. As the fact that the most damage is created in the 135° plies was previously reported in the literature [46], [47],  $S_{sk}$  is considered an effective parameter which is able to link the subsurface damage to surface metrics results for 135° fibre orientation.

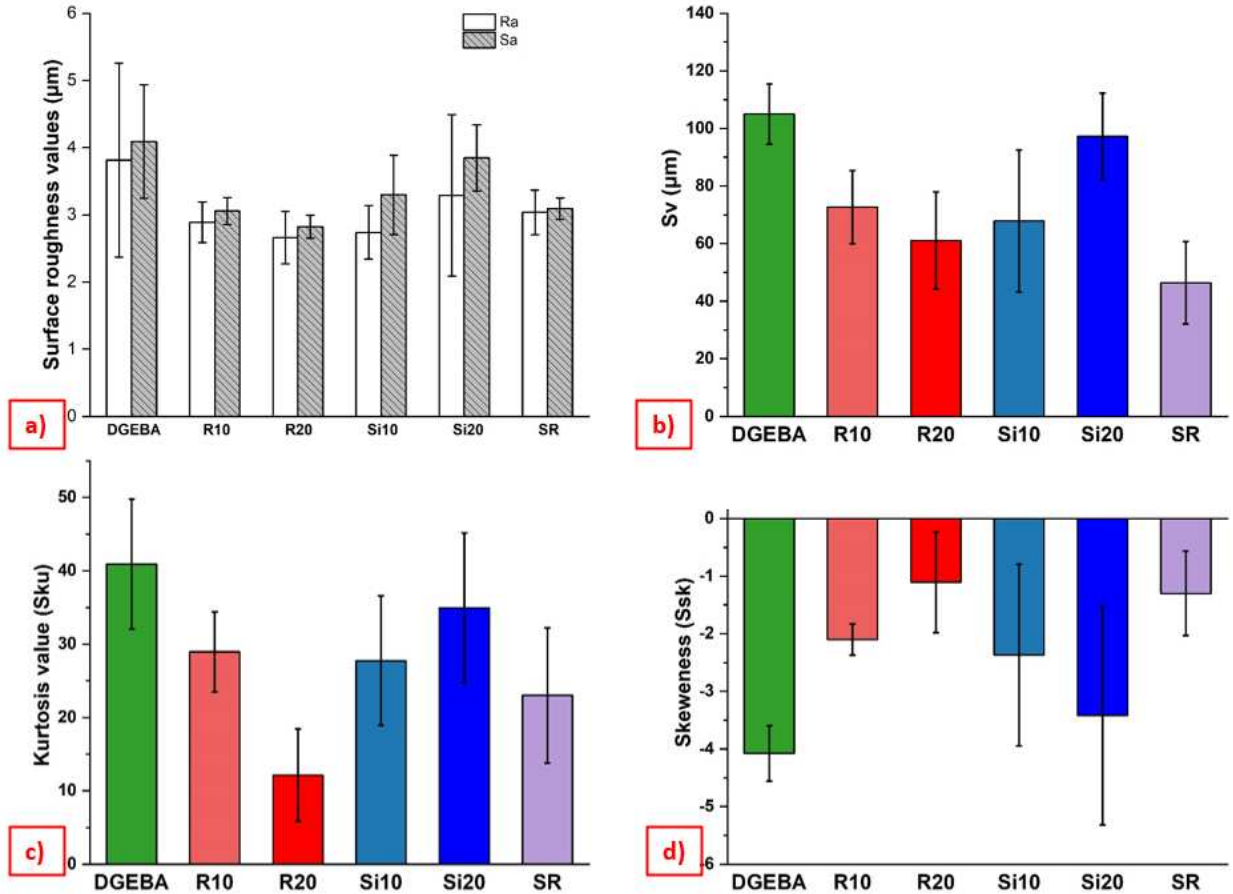


Figure 11 - Surface metrics measurements a) Surface roughness ( $R_a$ ,  $S_a$ ) b) Maximum valley depth ( $S_v$ ) c) Kurtosis ( $S_{ku}$ ) d) Skewness ( $S_{sk}$ )

### 3.6 Surface morphology assessment

Even though the machined surfaces showed significant smearing across all fibre orientations, various craters and material pull-out regions were used for fractographic analysis. Material pull-out regions and fibre-matrix debonding are observed for DGEBA and silica sample (Figure 12 – a, b)). Moreover, the fractured fibres show a clean surface which leads to the conclusion that the composite material failed at the interface region between the fibre and matrix. On the other hand, fractured material of R20 sample (Figure 12 – c)) showed fibres with matrix attached, which indicates that polymer debonding did not occur fully. The debonding is directly related to the fibre and matrix adhesion and the particle reinforcement of the epoxy does not have a significant role in the individual fibre toughening mechanism (e.g. fibre debonding, fibre pull-out). However, the presence of rubber microparticles and their subsequent toughening

mechanism, facilitated the fracture energy dissipation, which ultimately limited the fibre debonding and pull-out.

The principal toughening mechanism of rubber micro-particle and silica nanoparticle were previously demonstrated in the literature [23], [24], [28], [29], [38] and identified in the machined surface micrographs. High-resolution FEG SEM images of the rubber machined surface (Figure 13 – a)) shows that the particles cavitate. This is followed by plastic void growth of the polymer matrix. The original mean diameter of the rubber micro-particles was  $0.54 \mu\text{m}$  [28], while the cavitated areas were measured to be  $1.02 \pm 0.16 \mu\text{m}$ . Plastic deformation of the epoxy matrix is visible on the edge of the voids generated on the polymer matrix surface due to the cavitation process (Figure 13 – b)). It is also noticed that fibres are attached to the machined surface and are still encased in epoxy matrix, which further highlights the fact that fibre-matrix interface failure does not occur in rubber-modified samples. The rubber toughening mechanism allows the fracture energy to be dissipated, this limits the extent of subsurface damage from the compression induced by the flank face. These are correlated with the low oscillations of cutting force signal shown in Figure 2 – a).

High-magnification FEG SEM images of Si20 fractured surface (Figure 14 –a)) clearly illustrate the fibre pull-out and fibre-matrix debonding. The fractured surface of the matrix is relatively smooth, which is typical for a thermoset polymer. Similar features were found on high-magnification images of unmodified epoxy composite. Feather markings are observed, which are caused by crack forking due to the high energy associated with the relatively fast crack growth. Again, this was previously identified and is typical for a brittle epoxy material [23]. The presence of voids and silica nanoparticles on the high-resolution image indicates that plastic void growth of the material was initiated by the debonding of silica nanoparticles (Figure 14 –b)). Even though the samples were gold coated prior to SEM analysis, the voids and silica nanoparticles were not observed on the coated surfaces of unmodified epoxy composite. This shows that the identified voids are not an artefact of the applied gold coating. The measured voids have a diameter of  $39 \pm 4.53 \text{ nm}$ , while the silica nanoparticles are within the range of 20-25 nm. However, it can be seen that

not all particles initiated the void growth mechanism. It has been previously reported that only a fraction of the nanoparticles debond [23], [25], [29] and the considerable difficulty of quantifying the number of debonded particles. Hsieh et al. [25] discussed the reasons for the incomplete debonding of silica, namely (i) a purely statistical aspect of the fracture process (ii) that once a silica nanoparticle, or group of such particles, have debonded and the epoxy polymer undergoes plastic void growth, then the stress which drives such a mechanism is relieved in the adjacent region. The general conclusion is that if only a fraction of particles initiate plastic void growth, the toughening mechanism will be affected, thus decreasing the expected fracture toughness of the silica modified epoxy composite. Thus, the identified silica-toughening mechanism proved ineffective in the machining of CFRPs in terms of reducing machining induced damage and reducing cutting forces in comparison to rubber micro-particles.

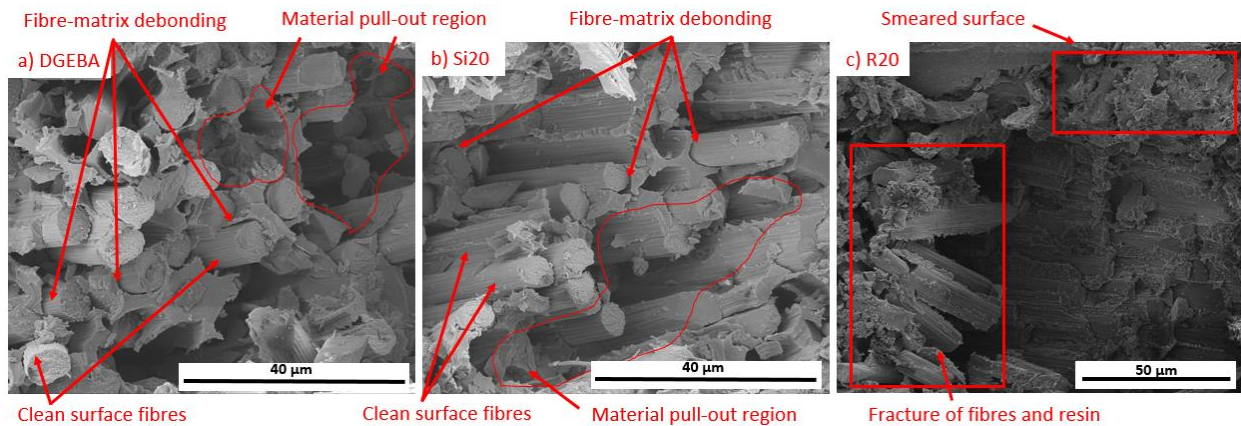


Figure 12 – Typical micrographs of machined surface of a) DGEBA b) Si20 and c) R20 samples, where ‘Clean surface fibres’ means the fibres have debonded from the matrix by adhesive failure

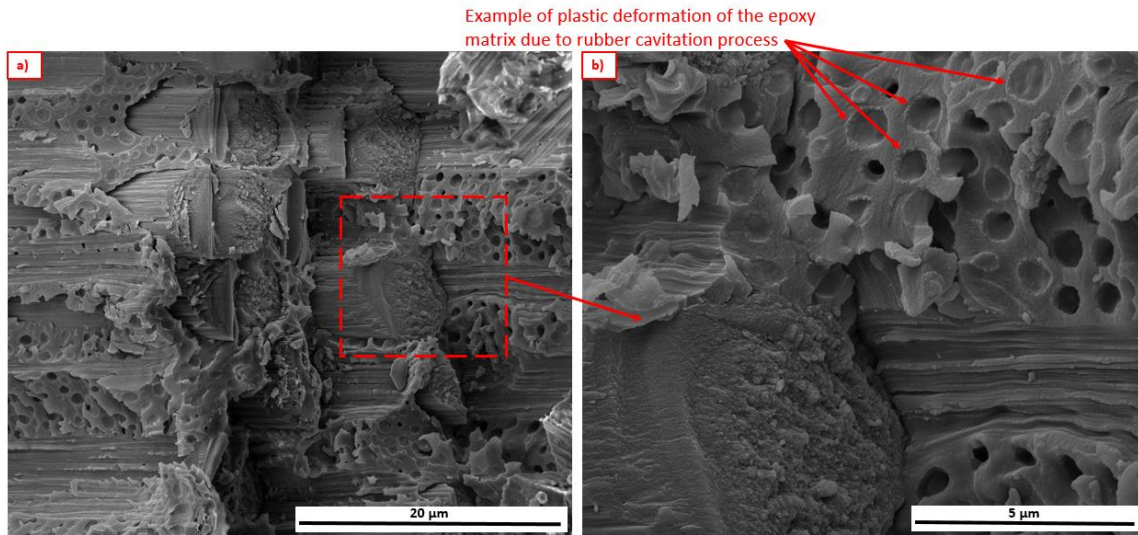


Figure 13 - High-resolution FEG-SEM micrographs of R20 machined surface a) Fibre and rubber cavitation process artefacts b) High-magnification example of plastic deformation of matrix due to rubber cavitation process, where rectangle shows a fibre bonded to the surrounding matrix

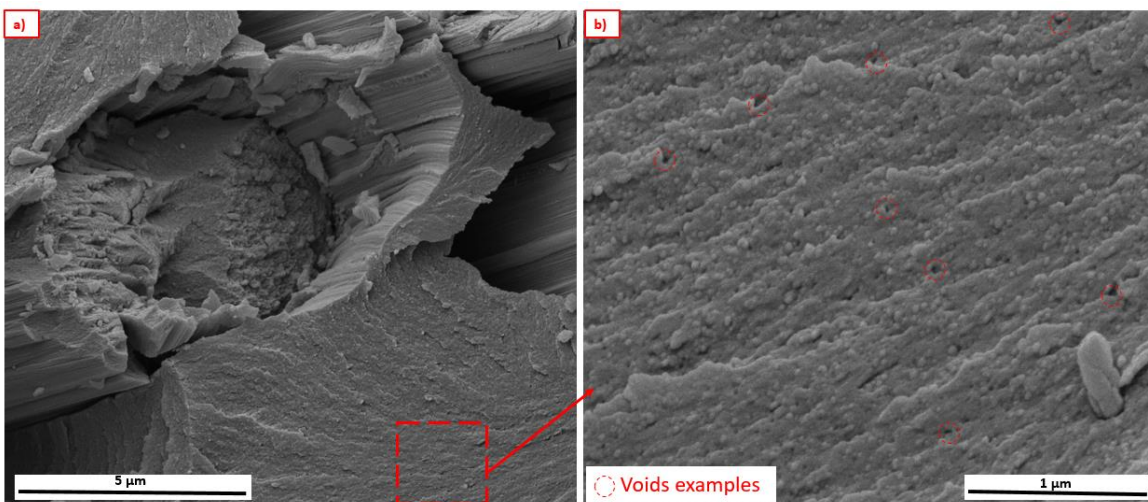


Figure 14 – High-resolution FEG-SEM micrographs of Si20 machined surface a) Fibre pull-out and fibre-matrix debonding b) Debonding of silica nanoparticles

## 4. Conclusions

This paper develops the understanding of the effects of silica nanoparticles and rubber microparticles in the material removal mechanism and the subsequent machining induced damage during orthogonal cutting of epoxy modified CFRPs. The addition of these particles has a controlling influence over the subsurface damage of the machined samples. The main conclusions are listed below:

- The lowest average cutting force was recorded for rubber modified samples, followed by silica and then by unmodified epoxy CFRPs. Rubber modified samples showed a stable cutting force, with regular oscillations, compared with the higher, more random oscillations experienced by unmodified and silica reinforced specimens.
- The presence of rubber microparticles increased the elastic recovery of the material, which resulted in the largest springback measured for all samples. The low magnitude of cutting forces was correlated with the lower depth of cut measured and reduced subsurface damage for rubber-modified samples.
- Strain map contours illustrate that material deformation in the chip formation zone is characterised by two zones, one that is extended ahead of the cutting tool for DGEBA and silica samples ( $> 100 \mu\text{m}$ ) and one that penetrates approximately  $45^\circ$  into the subsurface, compared to more localised contours of rubber-modified samples, in front and below the cutting tool.
- The material removal mechanism and subsequent machining induced damage for  $45^\circ$ ,  $90^\circ$  and  $135^\circ$  fibre orientation are affected by the presence of fillers. Rubber modified samples (R20) show the least subsurface damage (75% decrease for  $45^\circ$  plies, 66% decrease for  $90^\circ$  plies and 21% decrease for  $135^\circ$  plies) and measured areal damage (77% decrease for  $45^\circ$  plies, 60% decrease for  $90^\circ$  plies and 64% decrease for  $135^\circ$  plies) compared to DGEBA samples. A 50.8% decrease in surface craters is found between R20 and DGEBA samples in  $135^\circ$  plies. No notable difference was found for subsurface damage measurements in  $0^\circ$  plies.
- Surface metrics were found to be in good agreement with subsurface damage results, however, surface metric assessment of the machined surfaces is insufficient to fully characterise damage occurring during cutting.
- All of the above were linked to the particle toughening mechanism. This was found to take place during cutting, as particle cavitation for rubber microparticles and debonding for silica nanoparticles.

- Rubber toughening mechanism ensured an efficient energy dissipation mechanism limiting crack propagation and the extent of subsurface damage. The brittle state of epoxy matrix and the fact that not all silica nanoparticles debonded in the silica toughening process resulted in fibre pull-out and matrix-fibre debonding which proved ineffective in reducing the machining induced damage. Further studies will investigate the effect of reinforcement particles in an industrial machining process where higher feed rates result in higher strain rates and higher temperatures, which could lead to different damage and cutting mechanics.

## Acknowledgments

The authors would like to acknowledge the EPSRC Industrial Doctorate Centre in Machining Science (EP/L016257/1) for the funding of this work and to Huntsman, UK for the supply of the base epoxy resin. We also acknowledge The University of Sheffield Tomography Centre (STC) and its funding from EPSRC (EP/T006390/1).

## References

- [1] D. R. Tenney, J. Davis John G., N. J. Johnston, R. B. Pipes, and J. F. McGuire, “Structural Framework for Flight I: NASA’s Role in Development of Advanced Composite Materials for Aircraft and Space Structures,” 2019. [Online]. Available: <https://ntrs.nasa.gov/search.jsp?R=20190002562%0Ahttps://ntrs.nasa.gov/search.jsp?R=20190002561>.
- [2] R. Bagheri, B. T. Marouf, and R. A. Pearson, “Rubber-toughened epoxies: A critical review,” *Polym. Rev.*, vol. 49, no. 3, pp. 201–225, 2009, doi: 10.1080/15583720903048227.
- [3] S. Sprenger, “Epoxy resins modified with elastomers and surface-modified silica nanoparticles,” *Polymer (Guildf)*, vol. 54, no. 18, pp. 4790–4797, 2013, doi: 10.1016/j.polymer.2013.06.011.
- [4] F. Hussain, M. Hojjati, M. Okamoto, and R. E. Gorga, “Review article: Polymer-matrix nanocomposites, processing, manufacturing, and application: An overview,” *J. Compos. Mater.*, vol. 40, no. 17, pp. 1511–1575, 2006, doi: 10.1177/0021998306067321.
- [5] J. Baur and E. Silverman, “Challenges and Opportunities in Multifunctional Nanocomposites Structures for Aerospace Applications,” *MRS Bull.*, vol. 32, no. April, pp. 328–334, 2007.
- [6] J. M. Garcés, D. J. Moll, J. Bicerano, R. Fibiger, and D. G. McLeod, “Polymeric nanocomposites for automotive applications,” *Adv. Mater.*, vol. 12, no. 23, pp. 1835–1839, 2000, doi: 10.1002/1521-4095(200012)12:23<1835::AID-ADMA1835>3.0.CO;2-T.

- [7] D. Feldman, "Polymer nanocomposites in medicine," *J. Macromol. Sci. Part A Pure Appl. Chem.*, vol. 53, no. 1, pp. 55–62, 2016, doi: 10.1080/10601325.2016.1110459.
- [8] H. Tang and H. A. Sodano, "High energy density nanocomposite capacitors using non-ferroelectric nanowires," *Appl. Phys. Lett.*, vol. 102, no. 6, p. 63901, 2013, doi: 10.1063/1.4792513.
- [9] Q. Y. Tang, Y. C. Chan, N. B. Wong, and R. Cheungc, "Surfactant-assisted processing of polyimide/multiwall carbon nanotube nanocomposites for microelectronics applications," *Polym. Int.*, vol. 59, no. 9, pp. 1240–1245, 2010, doi: 10.1002/pi.2855.
- [10] L. Mishnaevsky, K. Branner, H. N. Petersen, J. Beauson, M. McGugan, and B. F. Sørensen, "Materials for wind turbine blades: An overview," *Materials (Basel)*, vol. 10, no. 11, pp. 1–24, 2017, doi: 10.3390/ma10111285.
- [11] S. Ashworth *et al.*, "Varying CFRP workpiece temperature during slotting: Effects on surface metrics, cutting forces and chip geometry," *Procedia CIRP*, vol. 85, pp. 36–41, 2020, doi: 10.1016/j.procir.2019.09.021.
- [12] N. Duboust, M. Watson, M. Marshall, G. E. O'Donnel, and K. Kerrigan, "Towards intelligent CFRP composite machining: Surface analysis methods and statistical data analysis of machined fibre laminate surfaces," *Proc. Inst. Mech. Eng. Part B J. Eng. Manuf.*, no. October, 2020, doi: 10.1177/0954405420960920.
- [13] S. Ashworth *et al.*, "Effects of machine stiffness and cutting tool design on the surface quality and flexural strength of edge trimmed carbon fibre reinforced polymers," *Compos. Part A Appl. Sci. Manuf.*, vol. 119, no. January, pp. 88–100, 2019, doi: 10.1016/j.compositesa.2019.01.019.
- [14] M. Monoranu *et al.*, "A comparative study of the effects of milling and abrasive water jet cutting on flexural performance of CFRP," in *Procedia CIRP*, 2020, vol. 85, pp. 274–280, doi: 10.1016/j.procir.2019.09.036.
- [15] A. Koplev, A. Lystrup, and T. Vorm, "The cutting process, chips, and cutting forces in machining CFRP," *Composites*, vol. 14, pp. 371–376, 1983.
- [16] D. Wang, M. Ramulu, and D. Arola, "Orthogonal cutting mechanisms of graphite/ epoxy composite. II. Multi-directional laminate," *Int. J. Mach. Tools Manuf.*, vol. 35, no. 12, pp. 1639–1648, 1995.
- [17] D. Arola, M. Ramulu, and D. H. Wang, "Chip formation in orthogonal trimming of graphite/epoxy composite," *Compos. Part A Appl. Sci. Manuf.*, vol. 27, no. 2, pp. 121–133, 1996, doi: [https://doi.org/10.1016/1359-835X\(95\)00013-R](https://doi.org/10.1016/1359-835X(95)00013-R).
- [18] D. H. Wang, M. Ramulu, and D. Arola, "Orthogonal cutting mechanisms of graphite/epoxy composite. Part I: unidirectional laminate," *Int. J. Mach. Tools Manuf.*, vol. 35, no. 12, pp. 1623–1638, 1995, doi: 10.1016/0890-6955(95)00014-O.
- [19] X. M. Wang and L. C. Zhang, "An experimental investigation into the orthogonal cutting of unidirectional fibre reinforced plastics," *Int. J. Mach. Tools Manuf.*, vol. 43, no. 10, pp. 1015–1022, 2003, doi: [https://doi.org/10.1016/S0890-6955\(03\)00090-7](https://doi.org/10.1016/S0890-6955(03)00090-7).
- [20] Q. An, W. Ming, X. Cai, and M. Chen, "Study on the cutting mechanics characteristics of high-strength UD-CFRP laminates based on orthogonal cutting method," *Compos. Struct.*, vol. 131, pp. 374–383, Nov. 2015, doi: 10.1016/j.compstruct.2015.05.035.
- [21] Y. Su, "Effect of the cutting speed on the cutting mechanism in machining CFRP," *Compos.*

- Struct.*, vol. 220, no. March, pp. 662–676, 2019, doi: 10.1016/j.compstruct.2019.04.052.
- [22] R. K. Thakur and K. K. Singh, “Influence of fillers on polymeric composite during conventional machining processes: a review,” *J. Brazilian Soc. Mech. Sci. Eng.*, vol. 43, no. 2, 2021, doi: 10.1007/s40430-021-02813-z.
- [23] B. B. Johnsen, A. J. Kinloch, R. D. Mohammed, A. C. Taylor, and S. Sprenger, “Toughening mechanisms of nanoparticle-modified epoxy polymers,” *Polymer (Guildf.)*, vol. 48, no. 2, pp. 530–541, 2007, doi: 10.1016/j.polymer.2006.11.038.
- [24] Y. Huang and A. J. Kinloch, “The role of plastic void growth in the fracture of rubber-toughened epoxy polymers,” *J. Mater. Sci. Lett.*, vol. 11, no. 8, pp. 484–487, 1992, doi: 10.1007/BF00731112.
- [25] T. H. Hsieh, A. J. Kinloch, K. Masania, A. C. Taylor, and S. Sprenger, “The mechanisms and mechanics of the toughening of epoxy polymers modified with silica nanoparticles,” *Polymer (Guildf.)*, vol. 51, no. 26, pp. 6284–6294, 2010, doi: 10.1016/j.polymer.2010.10.048.
- [26] H.-Y. Liu, G.-T. Wang, and Y. Zeng, “On fracture toughness of nano-particle modified epoxy,” *Compos. Part B Eng.*, vol. 42, no. 8, pp. 2170–2175, Dec. 2011, doi: 10.1016/J.COMPOSITESB.2011.05.014.
- [27] S. Sprenger, “Improving mechanical properties of fiber-reinforced composites based on epoxy resins containing industrial surface-modified silica nanoparticles: Review and outlook,” *J. Compos. Mater.*, vol. 49, no. 1, pp. 53–63, 2015, doi: 10.1177/0021998313514260.
- [28] T. H. Hsieh, A. J. Kinloch, K. Masania, J. Sohn Lee, A. C. Taylor, and S. Sprenger, “The toughness of epoxy polymers and fibre composites modified with rubber microparticles and silica nanoparticles,” *J. Mater. Sci.*, vol. 45, no. 5, pp. 1193–1210, 2010, doi: 10.1007/s10853-009-4064-9.
- [29] D. Carolan, A. Ivankovic, A. J. Kinloch, S. Sprenger, and A. C. Taylor, “Toughened carbon fibre-reinforced polymer composites with nanoparticle-modified epoxy matrices,” *J. Mater. Sci.*, vol. 52, no. 3, pp. 1767–1788, 2017, doi: 10.1007/s10853-016-0468-5.
- [30] A. J. Kinloch, A. C. Taylor, M. Techapaitoon, W. S. Teo, and S. Sprenger, “From matrix nano-And micro-phase tougheners to composite macro-properties,” *Philos. Trans. R. Soc. A Math. Phys. Eng. Sci.*, vol. 374, no. 2071, 2016, doi: 10.1098/rsta.2015.0275.
- [31] “BSI. Plastics - Thermomechanical analysis (TMA) - Determination of coefficient of linear thermal expansion and glass transition temperature. ISO 11359-2: 1999.”
- [32] S. Ashworth, J. Rongong, P. Wilson, and J. Meredith, “Mechanical and damping properties of resin transfer moulded jute-carbon hybrid composites,” *Compos. Part B Eng.*, vol. 105, pp. 60–66, 2016, doi: <https://doi.org/10.1016/j.compositesb.2016.08.019>.
- [33] Y. Guo, W. D. Compton, and S. Chandrasekar, “In situ analysis of flow dynamics and deformation fields in cutting and sliding of metals,” *Proc. R. Soc. A Math. Phys. Eng. Sci.*, vol. 471, 2015.
- [34] “BSI. Geometrical product specifications (GPS) - Surface texture: Areal Part 2: terms, definitions and surface texture parameters. ISO 25178-2:2012.” .
- [35] “BSI. Geometrical Product Specifications (GPS) - Surface texture: Profile method - Rules and procedures for the assessment of surface texture. ISO 4288:1998.” .
- [36] “BSI. Geometric product specifications (GPS) – Surface texture: Profile method - nominal

characteristics of contact (stylus) instruments. ISO 3274:1998.” .

- [37] A.F.Yee and R. A. Pearson, “Toughening mechanisms in elastomer-modified epoxies,” vol. 21, pp. 2462–2474, 1986.
- [38] A. J. Kinloch, S. J. Shaw, D. A. Tod, and D. L. Hunston, “Deformation and fracture behaviour of a rubber-toughened epoxy: 1. Microstructure and fracture studies,” *Polymer (Guildf)*, vol. 24, no. 10, pp. 1341–1354, 1983, doi: 10.1016/0032-3861(83)90070-8.
- [39] M. Monoranu, H. Ghadbeigi, J. P. A. Fairclough, and K. Kerrigan, “Chip formation mechanism during orthogonal cutting of rubber microparticles and silica nanoparticles modified epoxy polymers,” in *9th CIRP Global Web Conference, accepted for publication*.
- [40] S. Ashworth *et al.*, “Epifluorescent microscopy of edge-trimmed carbon fibre-reinforced polymers: An alternative to computed tomography scanning,” *Adv. Compos. Lett.*, vol. 29, pp. 1–8, 2020, doi: 10.1177/2633366X20924676.
- [41] N. Nguyen-Dinh, C. Bouvet, and R. Zitoune, “Influence of machining damage generated during trimming of CFRP composite on the compressive strength,” *J. Compos. Mater.*, vol. 54, no. 11, pp. 1413–1430, 2020, doi: 10.1177/0021998319883335.
- [42] N. Nguyen-Dinh, R. Zitoune, C. Bouvet, and S. Leroux, “Surface integrity while trimming of composite structures: X-ray tomography analysis,” *Compos. Struct.*, vol. 210, no. December 2018, pp. 735–746, 2019, doi: 10.1016/j.compstruct.2018.12.006.
- [43] J. Sheikh-Ahmad, *Machining of polymer composites*. Springer Verlag, 2008.
- [44] F. ji Wang, J. wei Yin, J. wei Ma, Z. yuan Jia, F. Yang, and B. Niu, “Effects of cutting edge radius and fiber cutting angle on the cutting-induced surface damage in machining of unidirectional CFRP composite laminates,” *Int. J. Adv. Manuf. Technol.*, vol. 91, no. 9–12, pp. 3107–3120, 2017, doi: 10.1007/s00170-017-0023-9.
- [45] N. Duboust *et al.*, “An optical method for measuring surface roughness of machined carbon fibre-reinforced plastic composites,” *J. Compos. Mater.*, vol. 51, no. 3, pp. 289–302, 2017, doi: 10.1177/0021998316644849.
- [46] A. Cenna and P. Mathew, “Evaluation of cut quality of fibre- reinforced plastics--a review,” *Int. J. Mach. Tools Manuf.*, vol. 37, no. 6, pp. 723–736, 1997.
- [47] N. Duboust *et al.*, “Machining of Carbon Fibre: Optical Surface Damage Characterisation and Tool Wear Study,” *Procedia CIRP*, vol. 45, pp. 71–74, 2016, doi: 10.1016/j.procir.2016.02.170.